

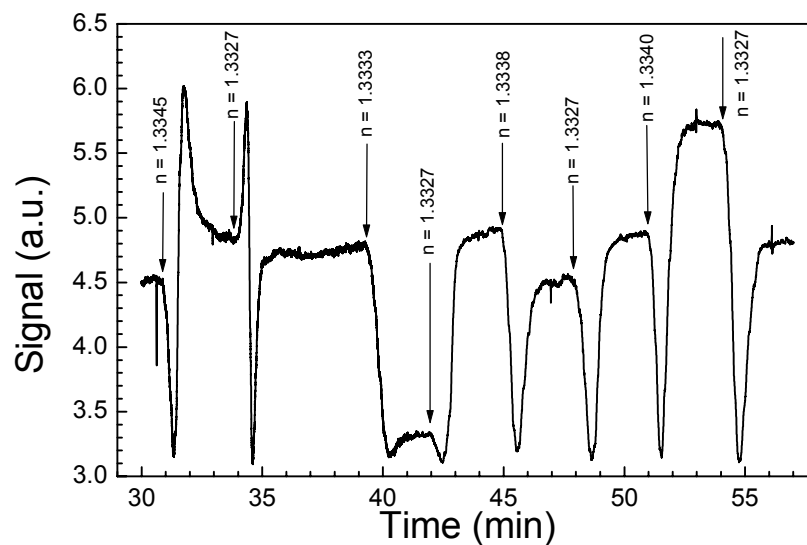
**Fig. 5.19:** Response of the MZI sensor as a function of the refractive index variation. The lines correspond to the theoretical simulation of the phase change: - (solid line)  $d_{ov} \sim 39$  nm; -- (dashed line)  $d_{ov} \sim 120$  nm.

Thence, optimizing the silicon nitride layer over the core so as to enhance the evanescent field propagation causes an increase of the sensitivity by an order of magnitude. However, it is still an order of magnitude above the required refractive index variation detection.

In chapter 2, it was observed that as the core thickness was reduced, an increase of the losses was straightforward. However, for values up to  $3\mu\text{m}$ , losses could be acceptable if a significant increase of the device properties were to be obtained. In this case, since a minor core means a higher evanescent field, MZI with waveguide cores of  $3\mu\text{m}$  should have better sensitivity. Experimental results shown in [3] proved that ARROW-A structures with a core of  $3\mu\text{m}$ , sensing layer of  $37\text{nm}$  and sensing region of  $15\text{mm}$  were able to detect refractive index variations of  $\Delta N=4.10^{-7}$ . Thus, with this configuration it could be possible to detect bio-molecular reactions. It has to be noted that its sensitivity is still a factor 3 below these of a silicon nitride TIR Mach-Zehnder Interferometer [5], nevertheless, due to the fact that the sensing region of ARROW MZI is 3 times larger, minimum refractive index variation that could be detected with the latter devices is an order of magnitude higher. Moreover, it has to be taken into account the previously described advantages that ARROW waveguides have as compared to TIR, as could be the much lower insertion losses and the align easiness.

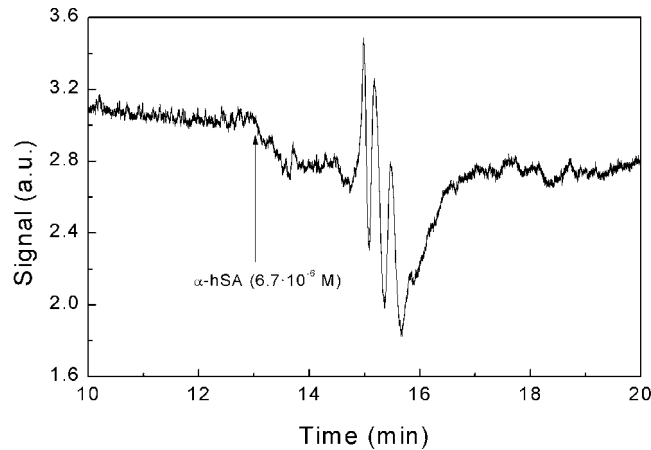


As a direct application for this highly sensitive interferometers, it could be used as a refractometer. In fig 5.20 it can be observed that the signal obtained at the sensor output strongly varies as a function of the refractive index and, perhaps what is more important, it is observed that the signal value obtained for a given refractive index is recovered after measuring a different sample, that is measurements done with the MZI are reversible.



**Fig. 5.20:** Response of the MZI sensor for glucose solutions with different refractive indexes.

As an example of biosensing application, the response to the physical adsorption of  $6.7 \cdot 10^{-6}$  M anti human serum albumin ( $\alpha$ -hSA) is presented in fig. 5.21. Measurements have been performed in phosphate buffered saline (PBS), with a pH of 7.35, at room temperature and maintaining a low flow rate (approximately 30  $\mu$ l/min). PBS has demonstrated to provide with the optimum pH and salinity conditions so as to keep the proteinic structure of the compounds unaltered. Antibodies form a monolayer with a thickness of around 10 nm by physical binding (electrostatic forces) to the waveguide surface. Causing a extremely small, however detectable, change in the signal at the device output.



**Fig. 5.21:** Signal response of the MZI sensor to the physical adsorption of an antibody monolayer (TE polarisation).

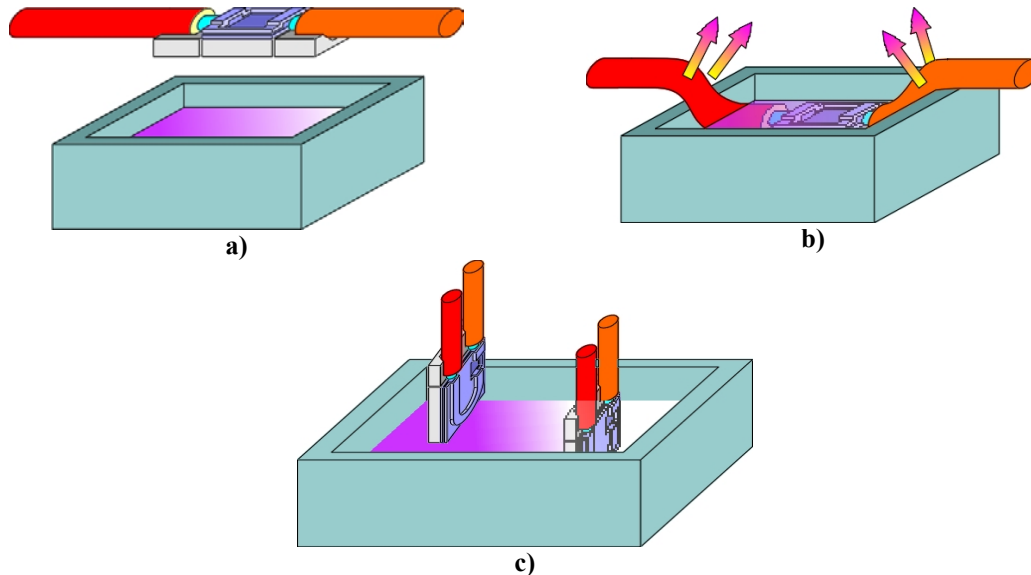
## 5.7 Absorption Sensor

The technological steps that allow obtaining absorption sensors are exactly equal as those presented for the MZI. The first mask would define the waveguide width, while the second would allow opening the passivation in the sensing region. This 1<sup>st</sup> generation of optochemical absorption sensors were successfully fabricated and tested [1], showing a sensitivity of  $10^{-4}$ M for  $K^+$  detection. The main drawback on that design was that input and output fiber optics were placed at both sides of the device. As can be seen in fig. 5.22a and 5.22b, after aligning and fixing the fiber optics, absorption sensors were submerged in a small volume of the solution to be measured. With this principle of operation, a crossed effect may occur: an unavoidable fiber optics bending is produced at the edges of the recipient. It causes the radiation of the higher modes in the fiber optics and a change in the light power. In order to assure that the power variation measured at the device output is only due to particle detection and not to fiber optics bending, the device has to be carefully placed on the sensing volume, trying to keep the fiber optics as straight as possible.

A second generation of this sensor was developed in order to overcome the double-facet polishing and the effect of the fiber optics bent. To do so, input and output waveguides were placed on the same side of the chip (fig. 5.22c). Light injected from the fiber optics was coupled to the input waveguide, which was bent 180° before injecting light into the sensing region. Finally, power was collected by a wider



waveguide and a multimode output fiber optics. With this configuration, fiber optics could remain straight during the measurement.



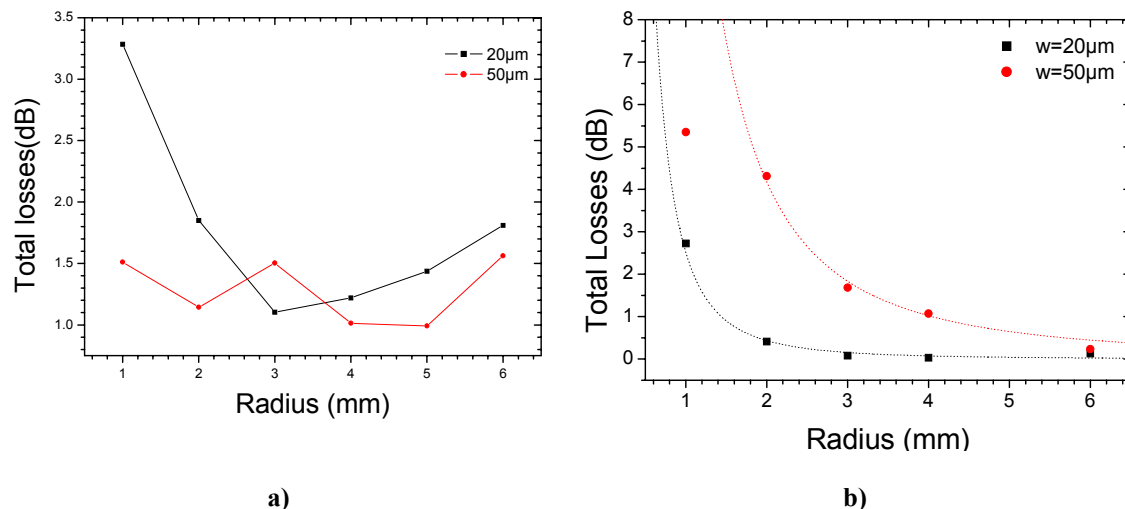
**Fig. 5.22:** Crossed effects on the 1<sup>st</sup> generation absorption sensor due to fiber optics bending. a) input and output waveguides where placed on both sides of the chip. b) When it was dipped in the solution, a fiber optic bent was produced, that caused fiber optics higher order modes to be radiative and polarization changes, resulting in a power decrease at the output due to fiber optics bent. c) 2<sup>nd</sup> generation optochemical sensors, where power was injected and collected by the same side of the chip, overcoming the bending effects.

In order to obtain the maximum available power at the sensing region, losses in the device must be minimized. According to [6], three main factors could be identified: attenuation (or intrinsic losses) both at the waveguide and at the bend region, radiation losses at the bending and losses produced at the straight-bend and bend-bend transitions. The sensor has been designed not to have this latter type of transitions, since it has been observed that losses at these points are 4 times higher as compared to straight-bend transition [6]. Thus, the optimum device would have a straight input waveguide, which is 180° bent. After this curvature, the waveguide is straight again (then, two straight-bend transition should be taken into account) and, after the sensing region, light is collected by a straight wider output waveguide.

At this point, it becomes necessary to analyze the effect that geometrical factors have on the losses, concretely, the radius and the width of the bend waveguide. Clearly, attenuation in bend waveguides would increase as the radius of curvature



increases, since the optical path is enlarged. However, as the radius increases, radiation losses are lower. Thus, a compromise between attenuation and radiation losses must be reached. Losses in  $180^\circ$  waveguides (without straight-bend transitions) with widths of  $20\mu\text{m}$  and  $50\mu\text{m}$  are presented in fig. 5.23a. As can be seen, losses in the wider waveguide are significantly lower as a function of the radius. From these results, it could be concluded that the wider waveguide should be the one with the bending, that is, that the sensing region should be placed near to the device input. However, when straight-bend transitions are studied (fig. 5.23b), it is observed that losses in the  $50\mu\text{m}$  waveguides are much higher. This can be associated to the fact that modes in a bend waveguide tend to displace towards the external part of the arc. Thus, the wider the waveguide, the larger the displacement. Thence, when bend-straight transition occurs, position and shape of the modes are so distorted that larger losses are produced.



**Fig. 5.23:** a) Total losses as a function of the radius in a  $180^\circ$  bent waveguide for two different waveguide widths. b) Transition losses as a function of the radius for two waveguide widths.

The second objective was to study the possibility of making a self-alignment system. By far, the most important bottleneck in integrated optics is the light coupling. Then, if waveguides could be easily aligned with fiber optics, this major drawback would be overcome. Moreover, it has to be noted that the sensing is done only in the sensor chip, then, it would be extremely useful to preserve the rest of the setup for further measurements. For that reason, a three-pieced setup was developed. The main idea was defining a setup that allowed changing and replacing sensors fastly and



without alignment. Sensor fabrication process starts as the MZI, with the 1<sup>st</sup> mask used for defining the core and the 2<sup>nd</sup> mask for obtaining the sensing region (table 5.9).


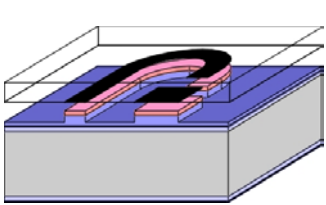


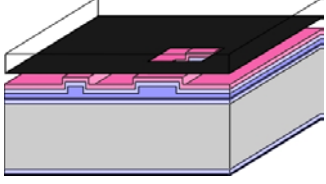

Scheme	Step properties	
	Silicon substrate. One-side polished, N-type, 4" diameter, 500µm thick <b>2<sup>nd</sup> cladding:</b> 2µm wet thermal silicon dioxide. n=1.46 <b>1<sup>st</sup> cladding:</b> 0.38µm LPCVD silicon nitride. n=2.00 <b>Core:</b> 4µm PECVD silicon oxide. n=1.48	
	CNM-120 GUIA mask: Definition of the rib structure 	<b>Mask</b> Input waveguide: 20µm Output Waveguide: 60µm Radius: 2,4,6mm <b>Step</b> 2µm positive photoresist 3.5µm SiO <sub>x</sub> RIE etching with CHF <sub>3</sub>
	<b>Passivation:</b> 2µm PECVD silicon oxide. n=1.46	
	CNM-120 SENS mask: Passivation opening 	<b>Mask</b> Sensing region: 500µm <b>Step</b> 2µm positive photoresist 2µm SiO <sub>x</sub> RIE etching with CHF <sub>3</sub>

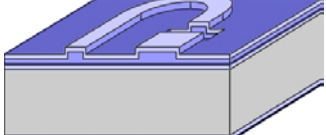
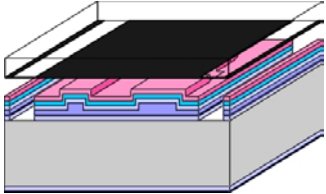
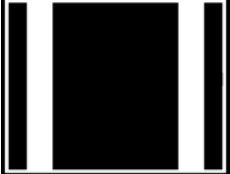
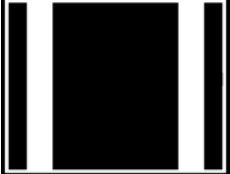
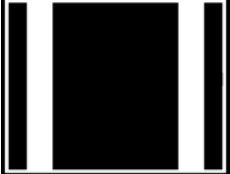
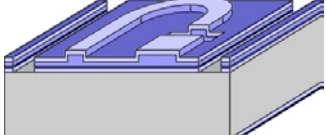
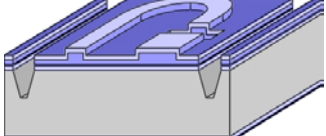
Table. 5.9: Technological steps used for the waveguide and the sensing region definition.

Once the passivation has been opened, following steps are focused on obtaining the self-aligned structure (table 5.10). This will be based on deep silicon wet etching on both sides of the sensor. This process will allow to obtaining smooth, accurately defined trenches in which the second part of the setup would be easily matched.

In order to define the deep trenches used for self-aligning purposes, a deep etch of the ARROW structure was required. Since this technological process needs large etching times, there are not any photoresist able to stand this process available at CNM. Thence, an aluminium mask has been used. To do so, 2µm aluminium has been sputtered and the self-aligned region is defined. After the elimination of the photoresist, the etching of the structure starts. Once the silicon substrate is reached, a wet etching in



KOH (that also etches the Al mask) is done until a depth of 250 $\mu$ m, ending the technological process for the sensor part.

Scheme	Step properties				
	Wafer after the sensor definition				
	<p data-bbox="579 703 1091 732"><b>CNM-120 ANCR</b> mask: self-aligning structure</p> <table border="1" data-bbox="579 736 1372 1088"> <tr> <td data-bbox="579 736 815 913">  </td> <td data-bbox="815 736 1372 875"> <p data-bbox="826 741 895 770"><b>Mask</b></p> <p data-bbox="826 770 986 799">Width: 724<math>\mu</math>m</p> </td> </tr> <tr> <td colspan="2" data-bbox="815 875 1372 1088"> <p data-bbox="826 880 879 909"><b>Step</b></p> <p data-bbox="826 909 1031 938">2<math>\mu</math>m Al Sputtering</p> <p data-bbox="826 938 1098 967">2<math>\mu</math>m Positive photoresist</p> <p data-bbox="826 967 995 996">2<math>\mu</math>m Al etching</p> <p data-bbox="826 996 1177 1025">2.5<math>\mu</math>m SiO<sub>x</sub> dry etch with CHF<sub>3</sub></p> <p data-bbox="826 1025 1217 1055">0.38<math>\mu</math>m Si<sub>3</sub>N<sub>4</sub> dry etch with SF<sub>6</sub>+He</p> <p data-bbox="826 1055 1150 1084">2<math>\mu</math>m SiO<sub>2</sub> dry etch with CHF<sub>3</sub></p> </td> </tr> </table>		<p data-bbox="826 741 895 770"><b>Mask</b></p> <p data-bbox="826 770 986 799">Width: 724<math>\mu</math>m</p>	<p data-bbox="826 880 879 909"><b>Step</b></p> <p data-bbox="826 909 1031 938">2<math>\mu</math>m Al Sputtering</p> <p data-bbox="826 938 1098 967">2<math>\mu</math>m Positive photoresist</p> <p data-bbox="826 967 995 996">2<math>\mu</math>m Al etching</p> <p data-bbox="826 996 1177 1025">2.5<math>\mu</math>m SiO<sub>x</sub> dry etch with CHF<sub>3</sub></p> <p data-bbox="826 1025 1217 1055">0.38<math>\mu</math>m Si<sub>3</sub>N<sub>4</sub> dry etch with SF<sub>6</sub>+He</p> <p data-bbox="826 1055 1150 1084">2<math>\mu</math>m SiO<sub>2</sub> dry etch with CHF<sub>3</sub></p>	
	<p data-bbox="826 741 895 770"><b>Mask</b></p> <p data-bbox="826 770 986 799">Width: 724<math>\mu</math>m</p>				
<p data-bbox="826 880 879 909"><b>Step</b></p> <p data-bbox="826 909 1031 938">2<math>\mu</math>m Al Sputtering</p> <p data-bbox="826 938 1098 967">2<math>\mu</math>m Positive photoresist</p> <p data-bbox="826 967 995 996">2<math>\mu</math>m Al etching</p> <p data-bbox="826 996 1177 1025">2.5<math>\mu</math>m SiO<sub>x</sub> dry etch with CHF<sub>3</sub></p> <p data-bbox="826 1025 1217 1055">0.38<math>\mu</math>m Si<sub>3</sub>N<sub>4</sub> dry etch with SF<sub>6</sub>+He</p> <p data-bbox="826 1055 1150 1084">2<math>\mu</math>m SiO<sub>2</sub> dry etch with CHF<sub>3</sub></p>					
	Wafer after the deep ARROW structure etching				
	250 $\mu$ m silicon wet etching in KOH				

**Table 5.10:** Definition of the deep trenches that would allow self aligning with the fiber optics.

The second part of the setup will allow aligning the sensor chip with the reaction chamber. Its technological steps are relatively simple (Table 5.11). However, they must have a high degree of accuracy in order to fit with the deep silicon trenches defined in the sensor device. Moreover, since the self-aligning structures have been done in the front side, this second piece should have a hole exactly in the sensing region, so as to permit the correct behavior of the device.